Soft Matter

Superhydrophobic μ-Pillars via Simple and Scalable SLA 3D-Printing: The Stair-Case Effect and their Wetting Models.

Journal:	*Soft Matter*
Manuscript ID	SM-ART-05-2021-000655.R1
Article Type:	Paper
Date Submitted by the Author:	01-Jul-2021
Complete List of Authors:	Bonilla-Cruz, José; Centro de Investigación en Materiales Avanzados Unidad Monterrey, Polymer Science Sy, Jo Ann; DOST Lara, Tania; CIMAV, Unidad Monterrey Gaxiola, Julio; CIMAV Unidad Monterrey Garcia, Vincent Joseph; Case Western Reserve University Basilia, Blessie; Mapua University, Materials Science and Engineering; Materials Science Division, Industrial Technology Development Institute, Department of Science and Technology Advincula, Rigoberto; Case Western Reserve University, Macromolecular Science and Eng.; University of Tennessee Knoxville College of Engineering; Oak Ridge National Laboratory

ARTICLE

Superhydrophobic µ-Pillars via Simple and Scalable SLA 3D-Printing: The Stair-Case Effect and their Wetting Models.

Received 00th January 20xx,
Accepted 00th January 20xx

DOI: 10.1039/x0xx00000x

José Bonilla-Cruz, Jo Ann C. Sy, Tania E. Lara-Ceniceros, Julio C. Gaxiola-López, Vincent García, Blessie Basilia, and Rigoberto C. Advincula*

In nature, superhydrophobic surfaces (SHS) exhibit microstructures with several roughness scales. Scalable fabrication and build-up along the X-Y plane represent the promise of 3D printing technology. Herein we report 3D printed microstructures with a dual roughness scale that achieves SHS using a readily available Formlabs stereolithography (SLA) printer. Pillar-like structures (PLS) arrangements with a wide range of geometrical shapes were 3D printed at three resolutions and two printing orientations. We discovered that a tilted printing direction enables a stair-case pattern on the µ-PLS surface, conferring them a µ-roughness which reduces the solid-liquid contact area. The programmed resolution governs the number of polymerized layers that give rise to the stepped pattern on the µ-PLS surfaces. However, this is reduced as the printing resolution increases. Also, all samples' experimental contact angles were consistent with theoretical predictions from Cassie-Baxter, Wenzel, and Nagayama wettability models. The underlying mechanisms and governing parameters were also discussed. It is believed that this work will enable scalable and high throughput roughness design in augmenting future 3D printing object applications.

Introduction

Nature has been an inexhaustible source of inspiration to study and emulate the superhydrophobic surface phenomena exhibited by several plants, animals, and insects.[1–7] Superhydrophobic surfaces (SHS) have drawn significant interest from both the industrial and the academic point of view due to their potential applications in the oil-water separation,[8] delayed ice accretion/lower ice adhesion,[9,10] self-cleaning surfaces,[11] fog-harvesting,[12] among others.[1,13–15] Furthermore, the SHS possess microstructures with a multiplicity of roughness-scales[16,17] in the micron and submicron range, thus minimizing the solid-liquid contact area (wettability) as well their surface energy.

Moreover, the sessile drop technique's contact angle (CA) measurement is a straightforward and standard method to study the surfaces' wettability phenomenon. Homogeneous wetting (Wenzel regime) occurs when a liquid completely penetrates between the protrusions or asperities down to the base of the rough surface;[18] meanwhile, Cassie-Baxter[19] regimen (C-B, heterogeneous wetting) occurs when the liquid is sitting on top of the surface, thus trapping air-pockets underneath the liquid,[6] giving droplet support and avoiding their intrusion. It is worth highlighting that even though the C-B theory has been used to explain the superhydrophobic effect for more than 80 years, several reports have questioned its relevance and applicability range, owing to substantial accuracy deviations (> 70 %) on the CAs predictions.[20–27]

Nevertheless, the Cassie-Baxter and Wenzel models are still widely used and accepted. It is worth mentioning that these models represent a good approximation if they are used in ideal conditions, being aware of their capabilities and limitations. McCarthy and Gao have described conditions where Cassie-Baxter and Wenzel equations represent a reasonable approximation or where they do not have any good performance.[20,21] On the other hand, new models have been developed to describe and predict the wetting phenomenon, including more factors that affect wettability.[19,28] Thus, a more detailed description can still be obtained, but more empirical data is required, turning them into even more complex models. Due to the latter, the Wenzel and Cassie-Baxter models still represent the most practical and used approximation method, as previously mentioned.

A SHS phenomenon is still operationally defined when its static CAs ($\theta_s \geq 150°$) is accompanied with a low hysteresis ($\theta_H < 10°$),

[a] *Advanced Functional Materials & Nanotechnology Group. Centro de Investigación en Materiales Avanzados S. C. (CIMAV-Subsede Monterrey), Av. Alianza Norte 202, Autopista Monterrey-Aeropuerto Km 10, PIIT, Apodaca-Nuevo León, México, C.P. 66628. Email: jose.bonilla@cimav.edu.mx Tel/Fax: +52 81 1156 0809.*
[b] *Industrial Technology Development Institute. Department of Science and Technology, Gen. Santos Ave., Bicutan, Taguig City 1631, Philippines.*
[c] *Department of Macromolecular Science and Engineering, Case Western Reserve University, Cleveland, OH, 44106, University of Tennessee, Knoxville, TN 37996, and Oak Ridge National Laboratory, Oak Ridge, TN 37830, USA Email: rca@case.edu*

Electronic Supplementary Information (ESI) available: **S1.** Theoretical Models. **Table S1.** Static, advancing, receding, and hysteresis contact angles (in deg.) corresponding to silanized micro-PLS, 3D printed at two orientations (tilted and horizontal), and at three resolutions (low, medium, and high). **Fig. S1**. Definition of the fraction of solid/liquid contact area, ϕ. **Fig. S2.** Micrographs by SEM and their CAs values corresponding to silanized µ-PLS 3D printed at medium resolution: a) horizontal orientation, b) tilted orientation. **Fig. S3.** a) Micrographs by SEM of silanized micro-PLS 3D-printed at tilted orientation and three printing resolutions (low, medium, and high), corresponding to geometrical shapes like a pine, cylindrical, and flat surfaces. b) Contact angle pictures corresponding to static, advancing, and receding contact angles. See DOI: 10.1039/x0xx00000x

wherein θ_H is the difference between the advancing (θ_A) and receding (θ_R) CAs. It is known that pillar-like structures (PLS) possess a high aspect ratio that, when ordered into arrays, can achieve isotropic CAs[29] as well as superomniphobic surfaces.[30] These protrusions or asperities from the surface can exhibit a wide range of geometries (roughly cubic, cylindrical, and conical in shape),[14,29,31] and spatial arrays that produce rough effects on the surface (macro-roughness). Typically, PLS are obtained through more sophisticated and labor-intensive lithography and stereolithography methods, which allows them to reach diameters (ϕ), heights (h), and distance between pillars (pitch, p) on the nanometric (< 0.1 µm) and micrometer (1-100 µm) scales.[29] Specifically, to achieve SHS based on PLS, a post-treatment (e.g., plasma etching, nanoparticles doping, etc.) may be necessary to produce micro- or nano-roughness on the surface of the pillars.

These days, stereolithographic 3D printing (µ-SLA) is considered a robust additive manufacturing (AM)[32,33] platform wherein 3-dimensional structures can be readily fabricated with high repeatability[34] and excellent fidelity[35] in a cost-effective manner. A very popular and inexpensive Formlabs™ SLA printer is readily available and is used in a lot of education and maker space facilities. Typically with SLA (a type of vat printing), a liquid crosslinker and oligomer, or telechelic polymer (functional-prepolymer dissolved in a mix of monomers), are selectively photopolymerized in a vat by a laser light-activated photoinitiator.[36] The laser-beam penetration level defines the layer-thickness obtained. Several polymer layers are built layer-by-layer on the X-Y plane, one on top of the other until the 3D object is obtained. Nonetheless, achieving surfaces with dual-roughness (one macro-roughness due to the pillar arrangements,[16] and another micro-roughness on the pillars' surface) when an object is simultaneously built along the X-Y plane is not well-reported with a common SLA printer, remaining as a major challenge for most commercial 3D printers.[7]

On the other hand, few studies have been reported using SLA printer to achieve SHS. Credi *et al.,*[37] in 2017 obtained hydrophobic and oleophobic surfaces from an array of cylindrical micro-pillars (h = 400 µm, ϕ ~ 100 µm, and p = 200, 250, and 350 µm) coated with perfluoropolyether. In 2019, artificial shark skin surfaces with microriblet features (friction factor ~ 0.04); and lotus leaf surfaces with micropillars (p = 300 µm) and CA < 150° also were designed by SLA.[38] Joyee *et al.,*[39] (2020) used a magnetic field-assisted multiscale SLA to build complex hierarchical structures from a mixture of polymer and particles (size ranging from nanometers to millimeters) were developed. Structures with conical protrusions were built, which exhibited CA < 150°. Recently, controlled wettability surfaces from an array surface of mushroom-head micropillars were investigated. Wettability was controlled by adjusting the h, p, and ϕ, thus obtaining CAs in the range of 55-171°.[40]

Herein we report a scalable process to achieve SHS with dual-roughness in one step (when an object is simultaneously built along the X-Y plane) using a readily available and inexpensive Formlabs 3D Printer. Furthermore, we report the fabrication of µ-PLS arrays having a wide range of shapes like a pine, sphere, spiral, stepped pyramid, cubic, mouse, mushroom, tulip, cone, cylinder, as well as a flat surface (control sample). All µ-PLS geometries were designed with ϕ = 400 µm, h = 900 µm, and p = 400 µm, and were 3D-printed by µ-SLA at two orientations (horizontal, and tilted at 33° along the X-Y plane) and three resolutions (low, LR; medium, MR; and high, HR) as shown in **Fig.1**.

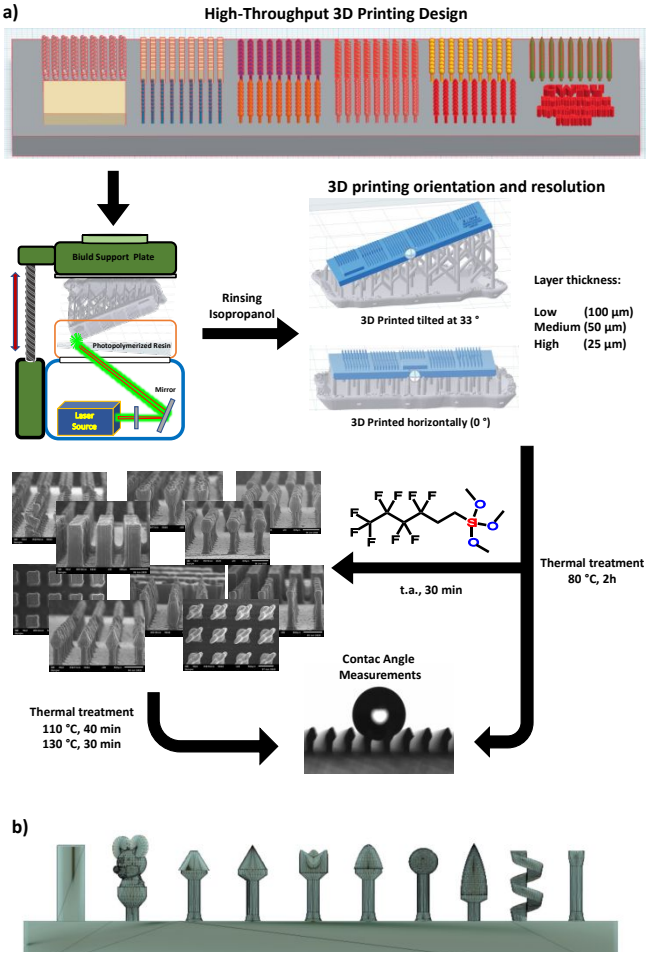

Fig. 1. a) Schematic procedure to get µ-PLS with dual-roughness and superhydrophobic behavior by high-throughput 3D printing; **b)** CAD design corresponding to a wide range of shapes studied (cubic, mouse, stepped pyramid, cone, tulip, mushroom, sphere, pine, spiral, and cylinder).

All 3D printed samples were cured and then silanized using a fluoroalkyl silane treatment. Also, another experimental set was performed without silanization treatment for comparison. CAs (θ_s, θ_A, θ_R, and θ_H) were measured by the sessile drop technique, and an average of five measurements was reported for all µ-PLS silanized and non-silanized regardless of the printing resolutions and orientation.

Further, predictions of the static CAs using the Cassie-Baxter, Wenzel, and Nagayama models were obtained considering the experimental top face surface area for each shape, and the results were comparatively plotted with the experimental data. Further, the tilted structures also were simulated, considering the projected solid area in contact with the liquid between 4 cylindrical µ-pillars, as is explained in Section **S1.2**

(Supplementary Information). This strategy reduces the top face surface area accordingly with the tilted printing at 33°. Thus, it is possible to get an increment on the predicted θ_s. ϕ_T is the new parameter that substitutes to ϕ in the Cassie-Baxter model (see **Fig. S1**, Supplementary Information) and it provokes a change in the fraction of the projected solid area in contact with the liquid for tilted structures, which is obtained as follows:

$$\phi_T = \phi \cos^2 \theta_P \quad \textbf{Equation 1}$$

Indeed, ϕ_T and ϕ are area-based factors, and the cosine of the printing angle (θ_P) affects the diameter of the μ-pillar; the latter becomes a quadratic argument in **Equation 1**. Thus, a good agreement with the experimental data was obtained where the tilted structures present higher static CAs than those horizontally printed. This was attributed to the decrement of the contact area (line) between the solid and the liquid produced by the stair-case effect introduced by the printing angle on the tilted structures.

Results and discussion

Using μ-SLA 3D Printing, several variables like the pillars shape, pitch, height, printing resolution, printing orientation, type of surface (flat or pillars), including coating (silanized or not silanized) can be investigated. We analyzed most of these variables by measuring the θ_s and θ_A using the sessile drop technique. Thus, all 3D-printed μ-PLS, without silanization treatment regardless of the printing orientation and printing resolution, exhibited a homogeneous wetting (Wenzel regimen), wherein the water droplet (5 μL) completely penetrates between pillars down to the base of the surface. These results were expected since the photopolymerized resin is slightly hydrophobic ($\theta_s \cong 112°$), and the distance between pillars (p = 400 μm) is too broad, avoiding holding the water droplet. Because of this, all the experiments discussed beyond this point will be focused only on the silanized structures.

3D-Printing Orientation Effect and The Double Roughness Scale. Static CAs values for all silanized μ-PLS are shown in **Fig. 2**, wherein most of the 3D-printed μ-PLS at a tilted orientation of 33° (solid circles) exhibited a superhydrophobic behavior reaching values of $166° \geq \theta_s \geq 150°$ under a Cassie-Baxter regimen. Interestingly, most of the 3D-printed samples at horizontal orientation (bicolored squares) showed a Cassie-Baxter regimen with hydrophobic CAs $150° > \theta_s \geq 140°$, and this effect was more evident at medium printing resolution (see **Table S1**, Supplementary Information). Further, at this printing orientation, only the μ-PL pyramidal shape showed a SHS behavior regardless of the printing resolution wherein the CAs $\theta_s \cong 156° \pm 1$.

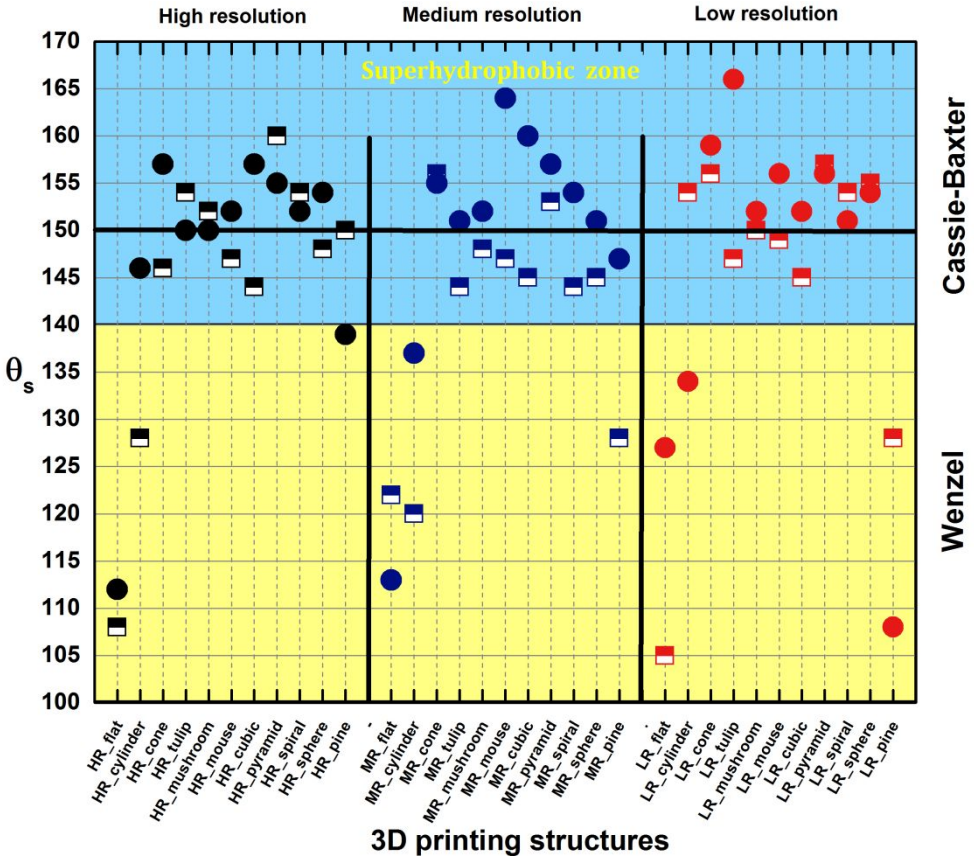

Fig. 2. High-throughput screening of static CAs (θ_s) corresponding to silanized μ- PLS with 10 different geometric shapes, 3D-printed at 3 resolutions (100 μm = LR, 50 μm = MR, and 25 μm = HR). Bicolored squares: 3D-printed at horizontal orientation; solid circles: 3D-printed tilted at 33°.

ARTICLE

At medium resolution seems to be that μ-PLS are correlated with the superhydrophobic CA; i.e., at tilted orientation, the CA decreases according to the following shapes: mouse > cubic > pyramid > cone > spiral > mushroom > sphere and tulip. In contrast, at horizontal orientation, these shapes exhibited almost the same hydrophobic CA. Nonetheless, at the high or low resolution, it not evident any correlation. On the other hand, **Fig. 3** clearly demonstrates the importance of 3D print at tilted orientation, since that most 3D printed μ-PLS at this orientation, achieving the Cassie-Baxter regimen with hydrophobic and superhydrophobic CAs (right-upper quadrant).

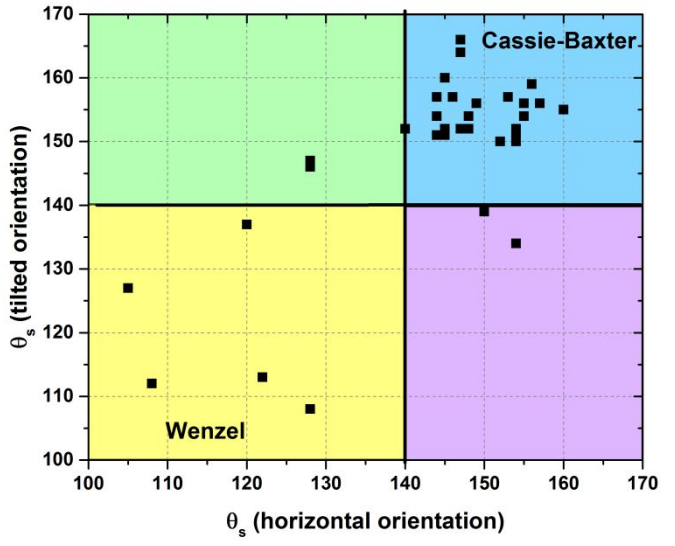

Fig. 3. Wenzel and Cassie-Baxter wettability regions for all 3D printed μ-PLS.

In the left lower quadrant, it is possible to observe the Wenzel regimen corresponding to μ-PLS with a shape like pine and cylinder, and flat surfaces. Finally, another useful analysis was performed plotting $\theta_{s,horizontal}$ / $\theta_{s,tilted}$ ($\theta_{s,h}$ / $\theta_{s,t}$) *vs.* the shape, as shown in **Fig. 4.** it is worth noting that three regions can be observed. First, Wenzel state (red squares) is consistently obtained when $0.88 > \theta_{s,h}/\theta_{s,t} > 1.05$. Remarkably, SHS regardless of the printing orientation (solid circles) were observed in the range of $1.05 > \theta_{s,h}/\theta_{s,t} \geq 0.96$. Thus, μ-PLS arrays having a shape like a tulip, mushroom, stepped pyramid, and spiral at HR; cone, mushroom, and stepped pyramid at MR; and cone, stepped pyramid, spiral, and sphere at LR, exhibited SHS in both printing orientations. In this region, μ-PLS arrays having a shape like a stepped pyramid exhibited SHS regardless of the printing resolution and printing orientation. Finally, in the range of $0.96 > \theta_{s,h}/\theta_{s,t} \geq 0.88$, we observed all μ-PLS that produced SHS just only on the tilted orientation (bicolored circles): cone, mouse, cubic, and sphere in HR; tulip, mouse, cubic, spiral, and sphere at MR; and tulip, mushroom, mouse, and cubic at LR. In this case, μ-PLS arrays having a shape like a mouse and cubic present SHS regardless of the printing resolution and printing orientation. **Fig. S2** (Supplementary Information) summarize all micrographs by SEM and their CAs (θ_S, θ_R, θ_A) measurements corresponding to silanized μ-PLS 3D printed at tilted and horizontal orientation, at medium resolution.

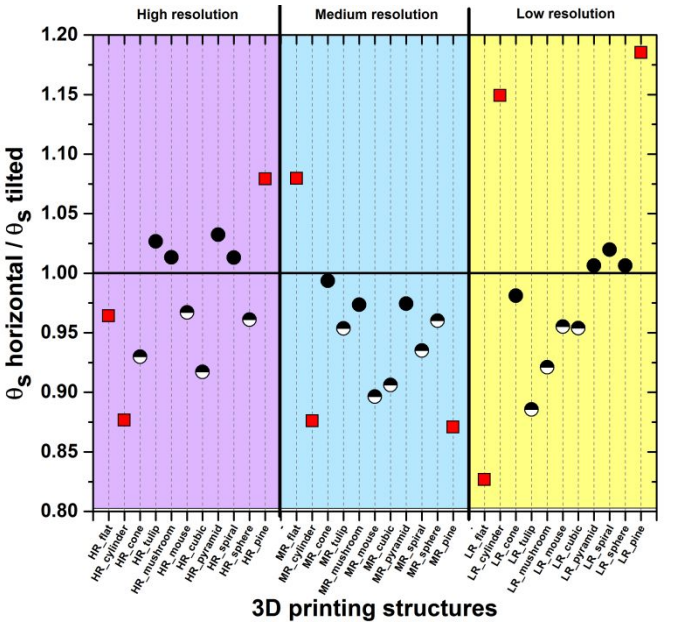

Fig. 4. ($\theta_{s,h}$ /$\theta_{s,t}$) *vs.* the shape. Solid circles: SHS obtained in a tilted as well in a horizontal printing orientation. Bicolored circles: SHS just only in the tilted orientation.

On the other hand, as was previously disclosed, Wenzel regimen ($\theta_s < 140°$) was systematically observed on μ-PLS with cylindrical and pine shapes regardless of the printing resolution, as shown in **Fig. S3**. Therefore, it appears that the 3D printing of μ-PLS with tilted orientation is always advantageous to achieving a SHS regardless of the shape or geometry. The central question that arises here is why?

The Formlabs μ-SLA produces a high degree of fidelity between the printed geometry and the design provided by CAD (geometry integrity) owing to the shapes being aligned along the build direction, which supposedly reduces the roughness on the surface. With the Formlabs SLA process, a 3D object under construction is introduced into the resin tank, wherein the laser light-beam produces a polymer layer in the X-Y direction. The

3D object is lifted orthogonally above the resin tank's surface for some seconds, later returning inside the tank again, and generates the next polymer layer. In this cyclic process, a meniscus of liquid resin is continuously formed between the adjacent layers during this lifting stage. This meniscus is also polymerized by the laser, filling the free volume between layers edges.[30,31] This effect reduces both the cusp height[35] (orthogonal distance between the tangent from two adjacent layers and their vertex) and the surface roughness, thus producing a 3D printed object with a slightly smooth surface.[42] Nonetheless, we observed by SEM microscopy that the 3D printing at tilted orientation always produces a stepped pattern on the μ-PLS surface, conferring them a micro-roughness (as illustrate the **Fig. 5**) which reduces the solid-liquid contact area that is crucial to get SHS.

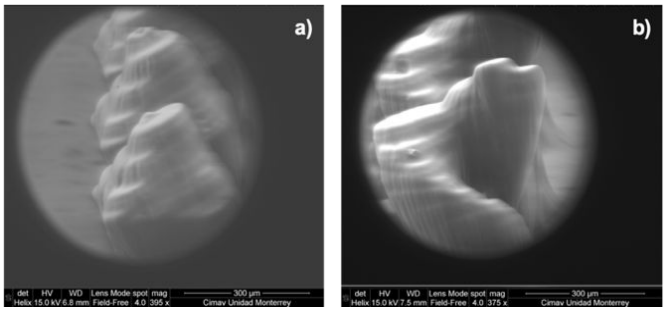

Fig. 5. Micrographs by SEM of micro-PLS 3D printed at tilted orientation and medium printing resolution, corresponding to shapes like a) stepped pyramid, b) spiral.

3D-Printing Resolution and the Stair-Case Effect. μ-PLS with geometries like pyramid, mushroom, tulip, spiral, and mouse exhibited a strong stair-case effect on their surfaces, showing the highest CAs. Here the printing resolution has been studied as shown in **Fig.6**. We found that it has a crucial role since it was possible to control the amount of the resolution variation steps when the μ-PLS were printing on a tilted orientation. Indeed, the steps obtained here are not synonymous with roughness to obtain SHS; nevertheless, they enable a type of double roughness scale.

The μ-pillars should constitute the macro-roughness (**Fig. 6**), and the asperities promoted by the stair-case effect should form the other scale of roughness at the micro-scale (see **Fig. 5**). Thus, at low resolution (layer height = 100 μm), we enable very long steps that produce μ-pillars with asperities, as shown in **Fig.6**. Meanwhile, at high resolution (layer height = 25 μm), we get shorter steps that produce μ-pillars with several asperities. Notice that the stair-case effect is geometrically dependent on the surface angle of the shape.[42] Thus, 3D-printing resolution governs the number of steps obtained by this stair-case effect, as shown in **Fig. 6**. This effect is lost as the printing resolution increases (a more significant number of polymer layers), which produces a smoother surface leading to a decreased SHS effect.

Interestingly in nature, several SHS have round-top protrusions, such as the shape of the lotus leaf.[4,43] This fact seems to suggest that this kind of geometric surface analogy also leads to SHS using μ-SLA 3D printing. We observed that not only μ-pillars with round-top surfaces produce SHS (such as a sphere, mushroom, or tulip), but the cubic and pyramid shapes promote SHS too with a tilted orientation. The best printability and SHS were found at medium resolution with $\theta_S \cong 160°$, which gave the most well-defined stair-case effect and fidelity of the pillar protrusion, as shown in **Fig. 6**.

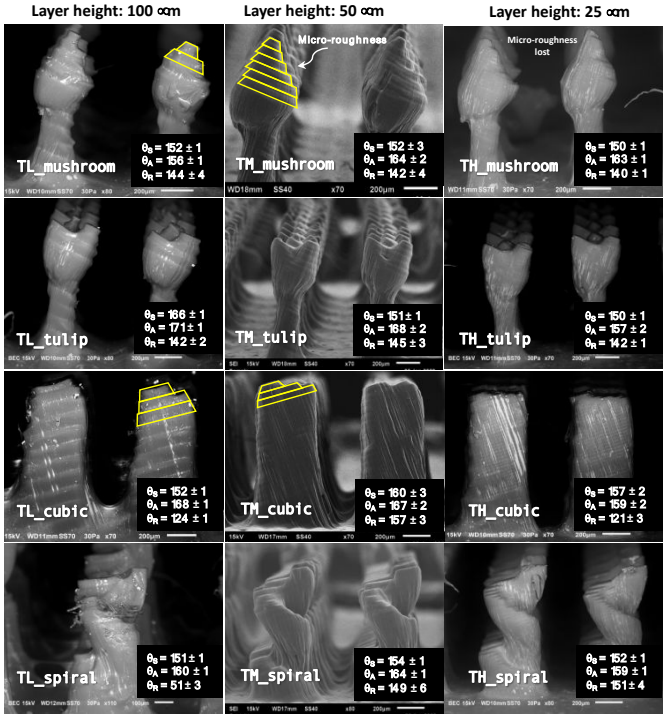

Fig. 6 Micrographs by SEM and their CAs (θ_S, θ_R, θ_A) measurements corresponds to silanized micro-PLS 3D printed at tilted at low, medium, and high resolution, having geometric shapes like a mushroom, tulip, cubic, and spiral.

Theoretical modelling *vs.* experimental data. A cylindrical pillar array with the same geometrical parameters reported (ϕ = 400 μm, h = 900 μm, and p = 400 μm) for the μ-PLS was utilized as an approximation to predict static CAs utilizing the Cassie-Baxter,[44] Wenzel[45] and Nagayama[28] models. The fitting for the several geometries studies was performed using the corrected effective projected area from the different 3D printing shapes in a tilted orientation the **Equation 1**. The effective areas were calculated using the CAD file to get the superficial contact area solid-liquid for each geometry using the Fusion 360 software, although more detailed protocols to calculate the effective area of irregular surfaces have been disclosed recently.[46–48]

For the case of μ-PLS 3D printed at 33° (as observed in **Fig. 7a**), the Cassie-Baxter model represent a good approximation for several geometries utilized, as spiral, pyramid, sphere, mouse, and mushroom, regardless of the printing resolution. The clear exceptions are the cone, the tulip, and the cubic geometries. Furthermore, the cylinder and pine shapes exhibited a big difference between experimental CAs and predicted CAs with the Cassie-Baxter model, except for LR and MR, respectively.

On the other hand, notice that the Nagayama model predictions resulted consistently with most part of the experimental results obtained, regardless of the printing resolution utilized. Nonetheless, the model is not consistent with the cone, tulip, and cubic geometries for all printing resolutions.

The consistency of the Nagayama model for the most of the geometries can be attributed to the versatility and wide range of applicability of the Nagayama model, including the intermediate wetting state. Besides, the predicted value for the Nagayama model is slightly lower than the value calculated with the Cassie-Baxter model due to the partial penetration of the droplet into the structure considered by the Nagayama model. It is worthwhile to mention that we used the effective wetting ratio, f = 2.2 (fractal dimension, D) reported before by Nagayama[28] for patterned microstructures.

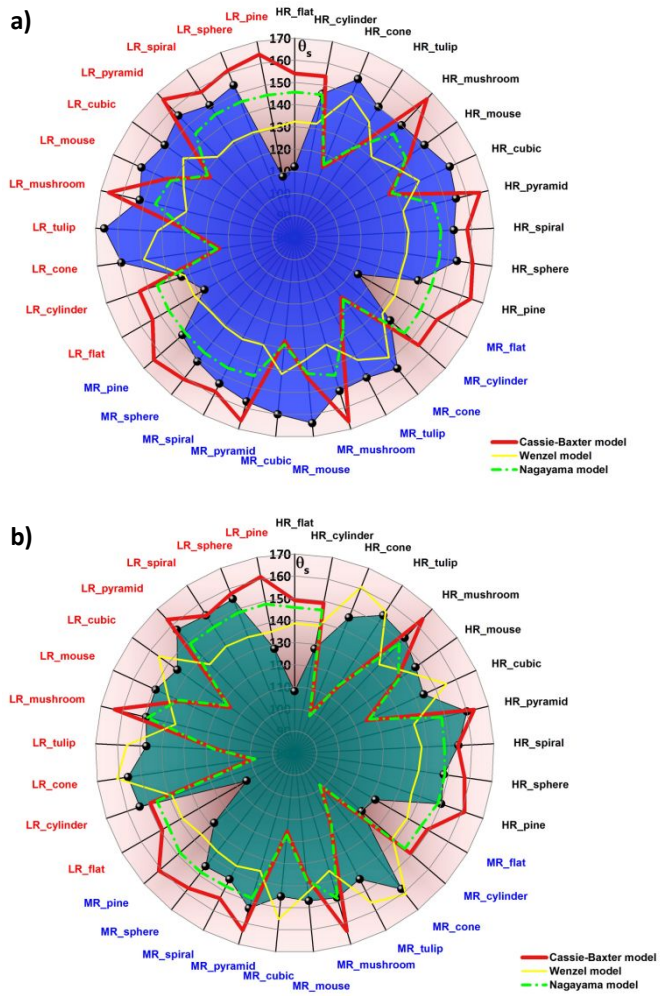

Fig. 7. Experimental static CAs (θ_s) compared with the theoretical predictions using the Cassie-Baxter, Wenzel, and Nagayama models. **a)** 3D-printed tilted orientation at 33°, **b)** 3D-printed at horizontal orientation.

In contrast, the Wenzel model is consistent with the cubic, tulip, pine, and cone geometries, regardless of the printing resolution, and with the medium and low-resolution of cylinder μ-PLS. From the geometries consistent with the Wenzel model, the pine presented a Wenzel regime under all printing resolutions, which is consistent with the predictions. Also, the cylinder presented Wenzel wetting state under low and medium resolution, which is in good agreement with predictions.

Further, to calculate the predicted static CA regarding the tilted structures, a new parameter ϕ_T related to the printing angle was introduced with the purpose to improve the results obtained for the cylindrical μ-pillar approximation. The modification introduced was the change of the solid/liquid contact area by a factor of the cosine of the printing angle (θ_P) as was discussed before. This factor tended to reduce the top surface area of the μ-pillars, as was shown in **equation 1**. The predicted static CAs for the tilted structures were higher than that predicted for the horizontal printed structures, which is in good agreement with the experimental results. There is a tendency for increments of the static CA for the tilted structures, as observed in **Fig. 7a**. This was attributed to the decrement of the contact area (line) between the solid and the liquid, produced by the stair-case effect, which was induced by the 3D printing tilted orientation at 33°.

Additionally, as can be observed in **Fig. 7b** (θ_s for μ-PLS 3D printed horizontally), the Cassie-Baxter model tended to be consistent with the pyramid, spiral, sphere, mushroom, and mouse geometries regardless of the printing resolution utilized. This is attributed to the homogeneous chemical composition and roughness of these surfaces provoked by the stair-case effect, where the contact area reflects the ground-state energies of the contact lines and the transitions between them, as was demonstrated by McCarthy and Gao.[20] Furthermore, the Nagayama model was also consistent with the pyramid, spiral, sphere, mushroom, and mouse geometries, which can be due to the presence of an intermediate wetting state on these geometries. However, the CAs values predicted with the Cassie-Baxter model are higher compared with the Nagayama model predictions. On the other hand, the Wenzel model predicted static CA slightly higher than the static CA experimentally obtained for the flat surfaces, as expected. This is attributed to the roughness ratio that portents hydrophobicity due to the presence of roughness and is absent on a flat surface.

Conclusions

In summary, using a fast and affordable SLA 3D printer, it is possible to achieve an SHS effect from variants of μ-PLS with a tilted orientation and defined resolution. The dual roughness-scale is achieved simultaneously with building the object along the X-Y plane. Thus, 3D printing and CAD shape prototyping were utilized for the high-throughput and scalable design screening of potential SHS effects that can be obtained in a one-step fabrication. Static CAs obtained for all samples were consistent with the theoretical predictions using several wettability theories. In the future, it is possible to incorporate these optimized surface design features in other SLA methods as part of a finished surface in one-step 3D printing. This will enable scalable and high throughput roughness design in

augmenting 3D printing object applications, including oil-water separation, selective filtration, low ice adhesion, self-cleaning surfaces, corrosion, moisture/fog harvesting.

Experimental Part

High-Throughput 3D Printing µ-pillars.

Several µ-PLS arrays having a wide range of shapes like a pine, sphere, spiral, stepped pyramid, cubic, mouse, mushroom, tulip, cone, cylinder, as well as a flat surface (control sample), were drawn in a three-dimensional computer-aided-design (CAD) model (tinkercad® 3D workflow from Autodesk®). The model designed was saved as stereolithography tessellation language (.stl file). The pillars' height was ~ 900 µm; the bottom distance between pillars was fixed at 400 µm, whereas the pitch (distance between heads) was ~ 400 µm. Polymeric µ-PLS arrays were 3D printed by stereolithography (SLA) using a 3D-printer desktop Formlabs-Form2® equipped with a 405 nm violet laser (Class 1) and a power source of 250 mW. Two printing orientations (horizontal 0° and tilted at 33°) and three printing resolutions (layer height: 100, 50, and 25 µm, respectively) were investigated. Clear resin (Formlabs, Somerville, MA, USA) was used as a photopolymerizable resin. All samples obtained here were cured at 80 °C in a convection oven for 2h; afterward were silanized by submerging them in 1H,1H,2H,2H-perfluorohexyl-trimethoxysilane, $C_6F_9H_4Si(OCH_3)_3$, (Gelest, Inc.) for 30 min. Finally, all silanized samples were dried for 40 min to 110 °C and then heated at 130 °C for 30 min in a convection oven. The apparent CAs for all silanized and non-silanized samples were carried out using a KSVCAM200 optical contact angle goniometer. Multiple measurements were taken, depositing 5 µL drops of DI water on each sample to acquire the θ_s, and 10 µL drops of DI water to get the advancing CA (θ_A). Dynamic CA (advancing θ_A, and receding θ_R) were performed using the increasing-decreasing method.[49] Scanning electron microscopy (SEM) was performed using a Jeol JCM-6510 and Jeol 6010 (low-vacuum) microscopes, operating at 15kV to observe the quality of 3D printing, as well as to analyze the roughness obtained.

Author Contributions

CRediT (Contributor Roles Taxonomy)

José Bonilla-Cruz, Jo Ann C. Sy, Tania E. Lara-Ceniceros, Julio C. Gaxiola-López, and Vincent García: conceptualization, formal analysis, investigation, methodology, validation, visualization, writing the original draft.

Blessie Basilia and Rigoberto C. Advincula: Conceptualization, funding acquisition, investigation, project administration, resources, supervision, writing-review & editing.

Conflicts of interest

There are no conflicts to declare.

Acknowledgments

J. Bonilla-Cruz and T. E. Lara-Ceniceros give thanks to CONACYT-México for the granting of a generous scholarship corresponding to the program "Supplementary Support for Sabbatical Stay Linked to the Consolidation of Research Groups" Modality: Abroad Sabbatical Stay. Also, the authors give thanks to Ing. Alberto Lara for the contact area measurements from CAD model.

Notes and references

1 B. Bhushan and Y. C. Jung, *Prog. Mater. Sci.*, 2011, **56**, 1–108.
2 X. Liu, H. Gu, M. Wang, X. Du, B. Gao, A. Elbaz, L. Sun, J. Liao, P. Xiao and Z. Gu, *Adv. Mater.*, 2018, **30**, 1–8.
3 T. B. H. Schroeder, J. Houghtaling, B. D. Wilts and M. Mayer, *Adv. Mater.*, , DOI:10.1002/adma.201705322.
4 Y. Sun and Z. Guo, *Nanoscale Horizons*, 2019, **4**, 52–76.
5 Y. Zuo, L. Zheng, C. Zhao and H. Liu, *Small*, 2019, **1903849**, 1–29.
6 J. Bico, U. Thiele and D. Quéré, *Colloids Surfaces A Physicochem. Eng. Asp.*, 2002, **206**, 41–46.
7 R. Jafari, C. Cloutier, A. Allahdini and G. Momen, *Int. J. Adv. Manuf. Technol.*, 2019, **103**, 1225–1238.
8 Y. Yang, X. Li, X. Zheng, Z. Chen, Q. Zhou and Y. Chen, *Adv. Mater.*, 2018, **30**, 1–11.
9 A. Davis, Y. H. Yeong, A. Steele, I. S. Bayer and E. Loth, *ACS Appl. Mater. Interfaces*, 2014, **6**, 9272–9279.
10 W. Shi, L. Wang, Z. Guo and Y. Zheng, *Adv. Mater. Interfaces*, 2015, **2**, 1–8.
11 Y. Lu, S. Sathasivam, J. Song, C. R. Crick, C. J. Carmalt and I. P. Parkin, *Science (80-.).*, 2015, **347**, 1132–1135.
12 B. Kang, J. Hyeon and H. So, *Appl. Surf. Sci.*, 2020, **499**, 143733.
13 A. Milionis, E. Loth and I. S. Bayer, *Adv. Colloid Interface Sci.*, 2016, **229**, 57–79.
14 E. Vazirinasab, R. Jafari and G. Momen, *Surf. Coatings Technol.*, 2018, **341**, 40–56.
15 H. Y. Erbil, *Langmuir*, 2020, **36**, 2493–2509.
16 E. Bittoun and A. Marmur, *Langmuir*, 2012, **28**, 13933–13942.
17 N. Michael and B. Bhushan, *Microelectron. Eng.*, 2007, **84**, 382–386.
18 H. Teisala, M. Tuominen, M. Aromaa, M. Stepien, J. M. Mäkelä, J. J. Saarinen, M. Toivakka and J. Kuusipalo, *Langmuir*, 2012, **28**, 3138–3145.
19 M. Im, H. Im, J. H. Lee, J. B. Yoon and Y. K. Choi, *Langmuir*, 2010, **26**, 17389–17397.
20 L. Gao and T. J. McCarthy, *Langmuir*, 2007, **23**, 3762–3765.
21 L. Gao and T. J. McCarthy, *Langmuir*, 2009, **25**, 14105–14115.
22 L. Gao and T. J. McCarthy, *Langmuir*, 2009, **25**, 7249–7255.
23 H. Y. Erbil and C. E. Cansoy, *Langmuir*, 2009, **25**, 14135–14145.
24 G. McHale, *Langmuir*, 2007, **23**, 8200–8205.
25 A. Marmur and E. Bittoun, *Langmuir*, 2009, **25**, 1277–1281.

26 H. Y. Erbil, *Surf. Sci. Rep.*, 2014, **69**, 325–365.
27 K.-Y. Law, *J. Phys. Chem. Lett.*, 2014, **5**, 686–688.
28 G. Nagayama and D. Zhang, *Soft Matter*, 2020, **16**, 3514–3521.
29 J. Y. Quek, C. L. Magee and H. Y. Low, *Langmuir*, 2017, **33**, 6902–6915.
30 H. Kim, H. Han, S. Lee, J. Woo, J. Seo and T. Lee, *ACS Appl. Mater. Interfaces*, 2019, **11**, 5484–5491.
31 J. Song, L. Huang, C. Zhao, S. Wu, H. Liu, Y. Lu, X. Deng, C. J. Carmalt, I. P. Parkin and Y. Sun, *ACS Appl. Mater. Interfaces*, 2019, **11**, 45345–45353.
32 J. R. C. Dizon, A. H. Espera, Q. Chen and R. C. Advincula, *Addit. Manuf.*, 2018, **20**, 44–67.
33 S. C. Ligon, R. Liska, J. Stampfl, M. Gurr and R. Mülhaupt, *Chem. Rev.*, 2017, **117**, 10212–10290.
34 H. Quan, T. Zhang, H. Xu, S. Luo, J. Nie and X. Zhu, *Bioact. Mater.*, 2020, **5**, 110–115.
35 M. Livesu, S. Ellero, J. Martínez, S. Lefebvre and M. Attene, *Comput. Graph. Forum*, 2017, **36**, 537–564.
36 A. Bagheri and J. Jin, *ACS Appl. Polym. Mater.*, 2019, **1**, 593–611.
37 C. Credi, M. Levi, S. Turri and G. Simeone, *Appl. Surf. Sci.*, 2017, **404**, 268–275.
38 Y. Li, H. Mao, P. Hu, M. Hermes, H. Lim, J. Yoon, M. Luhar, Y. Chen and W. Wu, *Adv. Mater. Technol.*, 2019, **4**, 1800638.
39 E. B. Joyee, A. Szmelter, D. Eddington and Y. Pan, *ACS Appl. Mater. Interfaces*, 2020, **12**, 42357–42368.
40 Q. Yin, Q. Guo, Z. Wang, Y. Chen, H. Duan and P. Cheng, *ACS Appl. Mater. Interfaces*, 2021, **13**, 1979–1987.
41 Y. Pan, X. Zhao, C. Zhou and Y. Chen, *J. Manuf. Process.*, 2012, **14**, 460–470.
42 P. E. Reeves and R. Cobb, *Rapid Prototyp. J.*, 1997, **3**, 20–31.
43 B. Bhushan and Y. C. Jung, *Prog. Mater. Sci.*, 2011, **56**, 1–108.
44 A. B. D. D. Cassie and S. Baxter, *Trans. Faraday Soc.*, 1944, **40**, 546–551.
45 R. N. Wenzel, *Ind. Eng. Chem.*, 1936, **28**, 988–994.
46 C. Sun, J. E. McClure, P. Mostaghimi, A. L. Herring, D. E. Meisenheimer, D. Wildenschild, S. Berg and R. T. Armstrong, *J. Colloid Interface Sci.*, 2020, **578**, 106–115.
47 C. Sun, J. E. McClure, P. Mostaghimi, A. L. Herring, M. Shabaninejad, S. Berg and R. T. Armstrong, *J. Colloid Interface Sci.*, 2020, **561**, 173–180.
48 H. T. Mahmood, E. Tsotsas and A. Kharaghani, *Transp. Porous Media*, , DOI:10.1007/s11242-021-01635-w.
49 J. Drelich, *Surf. Innov.*, 2013, **1**, 248–254.

